LUND
UNIVERSITY

Faculty of Engineering,
Department of Physics,
Division of Nuclear Physics.
Master's Programme of Science in Engineering,
Engineering Physics

Scattering Kernel Calculations for Liquid Para-Hydrogen Using Ring Polymer Molecular Dynamics

by

Pontus Nordin
April 2020

Supervisors:
Douglas Di Julio, Joakim Cederkäll

Examiner:
Bengt Martinsson

Abstract

The European Spallation Source will be a world leading neutron source available for a range of neutron scattering experiments in the scientific community. In order to accurately simulate the production of cold and thermal neutrons, an accurate calculation of the neutron cross section for the moderator materials is needed. The neutron cross sections used in the current simulation models for the liquid para-hydrogen moderator at the European Spallation Source are based on scattering kernels computed in NJOY. The scattering kernel calculations for para-hydrogen in NJOY are based on inputs from work that was carried out in the late 1980's. These approximations have yielded reasonable results and are therefore commonly used in cold neutron simulations. In more recent times, input for scattering kernel calculations has been provided by molecular modelling techniques. The present project investigated the methodology of using such techniques for para-hydrogen, namely quantum molecular dynamics. The method was bench-marked against results of other groups and was shown to give a resulting cross section comparable to experimental data as well as simulation data from other groups. Future work for improvements in the method are also discussed and presented.

Acknowledgements

I would like to extend my deepest thanks to my supervisor Douglas Di Julio for being a great supervisor and mentor throughout my thesis project. I also thank the Spallation Physics Group at the ESS for welcoming me into the group and brightening my duration at the ESS, as well as my university supervisor Joakim Cederkäll for valuable advice during the project.

I would also like to express my gratitude to the ESS for the generous funding received for the completion of this project.

Finally, special thanks to my best friend Audrey for supporting me in these stressful times and for graphical inputs to the report.

Contents

Chapter 1

Introduction

1.1 The European Spallation Source, ESS

The European Spallation Source (ESS) is currently under construction in Lund, Sweden. When it is finished it will be the world's brightest neutron source and will be available for a range of research areas doing neutron scattering experiments [1]. Neutron scattering is a method that can be used to examine material properties and structures. Because of the neutron's neutral charge, it interacts only with the nuclei of the atoms and can be used as a complementary method to x-ray scattering experiments. In order to be able to produce high quality scattering experiments, an intense source of neutrons is needed. The technique used at ESS to create neutrons is called spallation. In this method, protons are accelerated to high energies in a linear accelerator before colliding into a target material. In the collision, neutrons are stripped from the target material and spread away from the collision point, often with high energies. For most neutron scattering experiments, however, low energy neutrons are preferred. Therefore, spallation sources make use of a moderator, which is a volume of a material placed next to the spallation target. Typical neutron moderator materials include water, heavy water and hydrogen. The moderator material is chosen to slow down the neutrons coming from the target before they reach the guides that take them to the experimental stations. The slowing down, or cooling of the neutrons is done by letting the neutrons collide repeatedly with the molecules in the moderator. At each collision, a neutron deposits part of its energy to the moderator molecules, until in thermal equilibrium with the moderator material. To be able to calculate the final intensity and energy of the neutrons reaching the experimental stations, it is therefore of importance to be able to realistically simulate these collisions. For this reason, an accurate calculation of the neutron cross section for the moderator material is needed.

1.2 The ESS moderator

The novel design for the neutron moderator that will be used at the ESS uses a flat moderator with a 'butterfly' shape to increase the brightness at the experimental stations and is described by Zanini et al. [2]. The brightness of a neutron source is a characteristic property of the source, related to the number of neutrons available for the neutron scattering experiments. The design includes a pre-moderator filled with water and a cold moderator filled with liquid para-hydrogen. The pre-moderator sits closer to the target and acts like a middle step, bringing the neutrons from the MeV range right after the spallation, down to the thermal range of 20-100 meV. This is of importance because the neutron cross section of liquid hydrogen is dependent on the energy of the incoming neutrons. High energy neutrons have a relatively low probability of interacting with the hydrogen molecules, and by first letting the neutrons lose some of their energy in the water moderator, the efficiency of the hydrogen moderator is increased. Liquid para-hydrogen is a common choice for a cold moderator [2] and moderates the neutrons from the thermal range down to the cold range of < 5 meV. Furthermore, the butterfly design of the moderator includes both a cold moderator of hydrogen and a thermal moderator of water, giving a high brightness of both cold and thermal neutrons for the experimental stations. This gives a wider range of available neutron scattering experiments for the users.

1.3 Scattering kernels

The neutron cross section is calculated using the thermal scattering law (TSL), $S(\alpha, \beta)$, where α is the dimensionless momentum transfer in the scattering and β is the dimensionless energy transfer. Information about the neutron cross section is often stored in scattering kernels as tabulated values of $S(\alpha, \beta)$ for a range of α and β. A number of computer codes to calculate the TSL have been developed over the past 60 year, with the primary one being the LEAPR module in the NJOY code, developed by MacFarlane et al. [3]. A modification of the LEAPR module to account for low energy coherent inelastic scattering in liquid hydrogen has been developed by Márquez Damián et al. [5] based on the work by Granada and Gillete [6]. This modified version was used in the present project and will henceforth be referred to as the H2D2-model.

The scattering of neutrons at high energies (above a few eV) is not dependent on the chemical structures of the scattering material, however, at lower energies these structures start to play a role and, in order to properly model the scattering, knowledge of the structure and dynamics on a molecular level is needed. Earlier evaluations of the TSL relied on a number of approximations to account for these

molecular effects. Recent advancements in atomistic simulation techniques such as molecular dynamics (MD) and higher computing power of modern computers have made it possible to study the molecular effects in more detail. As a result, new methods to calculate the TSL using molecular simulation results have been developed. A recent report by the Nuclear Energy Agency discusses a number of these methods, developed by different research groups [4]. One of these methods, developed by Márquez Damián et al. [7], makes use of classical MD to simulate the scattering molecules and compute atomic correlation functions that are then used as an input to NJOY which calculates the TSL. This method is applied to water, however, for a quantum liquid such as liquid hydrogen, classical MD is not sufficient to incorporate the full dynamics of the system. A few groups, including Guarini et al. [8] and Miller and Manolopoulos [9], have showed that the use of quantum molecular dynamics (QMD) can be used to successfully compute atomic correlation functions for liquid hydrogen. Guarini et al. [8] also uses these correlation functions to compute the TSL directly without implementing it in NJOY. However, for this project it is deemed too computationally heavy for development of a scattering kernel. Instead, the method of Guarini et al. [8] using QMD, could be combined with the work of Márquez Damián et al. [7], thus implementing the atomic correlation functions from QMD into the standard methods for calculating the scattering kernels using NJOY. In this way it could be used as an ab initio method to calculate the neutron cross section. This would provide a more fundamental neutron cross section than what is currently used in simulations at the ESS and would as such be an upgrade to the current methods.

1.4 Objectives

The objective of this project was therefore to investigate the feasibility of implementing a new method to calculate the thermal scattering law, $S(\alpha, \beta)$, from quantum molecular dynamics simulations. The results were bench-marked against existing literature at each possible step of the calculations in order to make sure the method is correct and adaptable. The final cross section calculated through NJOY was compared to the cross section calculated with the current methods.

Chapter 2

Thermal neutron scattering

The neutrons escaping the spallation target can have high energies, in the MeV range [2]. Such high energy neutrons need to be slowed down before reaching the experimental stations and this energy range is therefore called the 'slowing-down region'. The interaction of neutrons in the slowing-down region with the moderator material can be modelled with simple, known theory [10] that will not be discussed further in the present report. When the neutrons are slowed down to energies below 1 eV they enter the 'thermal region', in which the neutron energies are similar to the thermal energies of the scattering nuclei. Now the nuclei can no longer be considered at rest, relative to the motion of the neutron, and the simple theory from the slowing-down region breaks down. At these energies the effect of the binding of the nuclei in molecules and solid crystal structures must also be taken into consideration. This is both with regards to the recoil of the molecule structure in the collisions, as well as possible interference effects arising due to the de Broglie wavelength of the neutron in the thermal region becoming comparable to the distances between atoms in the molecules. These effects in the thermal region only affect the neutron scattering. For the absorption cross sections, the changes are negligible and the same theory as in the slowing down region can be used [10]. Absorption will hence not be discuss further in the present report.

The thermal scattering is divided in two parts: elastic and inelastic scattering, which in turn can be either coherent or incoherent. Inelastic scattering is associated with an excitation or de-excitation of the scatterer. In the thermal region the neutrons don't have enough energy to excite the individual atom, however, if the atom is bound in a molecule or crystal structure, this system can have vibrational and rotational excitation modes in the thermal neutron energy range. In a liquid or gas, the excitation can also correspond to an atomic or molecular recoil motion, referred to as a translational excitation. A collision in

which the neutron gains or loses energy due to an excitation or de-excitation of the scatterer is described as thermal inelastic scattering. In thermal elastic scattering there are no such changes in the internal states of the scatterer, and as a consequence no change in the neutron's energy. It should be noted that this definition of thermal elastic scattering differs from the elastic scattering known for higher energy neutrons in which the neutron can loose energy in elastic scattering. This is because in thermal elastic scattering, the neutron interacts with an aggregate of atoms instead of individual atoms, thus the effective mass of the scatterer will be much greater than the neutron and will not lose energy in the collision [3,10]. It can be shown that for thermal scattering in liquids and gases there will be no elastic scattering [11], therefore elastic scattering will not be further considered in the present report.

2.1 Thermal scattering law

The double differential cross section, $\frac{d^2\sigma}{dE'd\mu}$, over the final state energy E' and the cosine of the scattering angle, μ [10,13], can be calculated from the thermal scattering law, $S(\alpha,\beta)$, from the following relationship [7],

$$\frac{d^2\sigma}{dE'd\mu} = \frac{\sigma_b}{2k_bT}\sqrt{\frac{E'}{E}}S(\alpha,\beta). \tag{2.1}$$

Here σ_b is the bound scattering cross section of the atom, k_b is Boltzmann's constant, T is the temperature and E and E' are the energies of the incident and outgoing neutron. $S(\alpha,\beta)$ is a function of the dimensionless momentum transfer, α, and the dimensionless energy transfer, β, given by the definitions in equation 2.2,

$$\alpha = \frac{E'+E-2\sqrt{EE'}\mu}{m/m_nk_bT}; \quad \beta = \frac{E'-E}{k_bT}, \tag{2.2}$$

where m is the mass of the scattering atom and m_n is the mass of the neutron. The thermal scattering law can also be written as a function of the momentum transfer, Q, and the energy transfer, $\hbar\omega$, where $\hbar$ is the reduced Planck's constant and

$$\omega = \frac{E'-E}{\hbar}.$$

The two functions are related by a scaling constant as

$$S(\alpha,\beta) = \frac{k_bT}{\hbar}S(Q,\omega). \tag{2.3}$$

The dimensionless quantities α and β can also be related to Q and ω as

$$\alpha = \frac{\hbar^2Q^2}{2mk_bT}, \quad \beta = \frac{\hbar\omega}{k_bT}. \tag{2.4}$$

2.1.1 Incoherent and coherent scattering

In thermal inelastic scattering, interference effects must be taken into account. This is because the de Broglie wavelength of the thermal neutrons are comparable to the distances between the atoms in the scatterer molecules. The de Broglie wavelength, λ, in ångström of a neutron with energy, E, in meV is given by [10]

$$\lambda = \frac{9.045}{\sqrt{E}}. \tag{2.5}$$

The molecular bond length in a hydrogen molecule is 0.74 ångström [12], and then by equation 2.5 this means neutrons of energy in the order of 3.5 meV would have the possibility to interfere. The general procedure of adding the interfering waves is the same as for scattering of light and the scattered waves are added in a coherent way with regard taken to their relative phases. Generally, the total cross section is given as a combination of a coherent part and an incoherent part, where the coherent scattering takes the interference into account and contains information about the interaction between atoms, while the incoherent scattering does not give interference effects and contain information about the properties of the individual atoms. The inelastic cross section can then be written as a sum of the coherent and the incoherent parts as

$$\frac{d^2\sigma}{dE'd\mu} = (\frac{d^2\sigma}{dE'd\mu})_{coh} + (\frac{d^2\sigma}{dE'd\mu})_{incoh}. \tag{2.6}$$

2.1.2 Self- and distinct dynamics

The thermal scattering law can be written as the Fourier transform in space and time of the pair distribution functions [10],

$$G(r,t) = G_s(r,t) + G_d(r,t), \tag{2.7}$$

containing information about the dynamics of the scattering material. If a scattering atom is located at the origin at the time $t = 0$, in the absence of quantum effects, $G(r,t)$ describes the probability that a second atom will be present at time t within a unit volume at position r. The 'self' part, $G_s(r,t)$, describes the probability that the second atom is the same (identical) as the first one, while the 'distinct' part, $G_d(r,t)$, describes the probability that the second atom is different than the first. Two Fourier transforms are then written, one for the total $G(r,t)$, and one for the self part as

$$\begin{aligned} S(Q,\omega) &= \frac{1}{2\pi}\int_{-\infty}^{\infty}\int e^{i(Qr-\omega t)}G(r,t)drdt, \\ S_s(Q,\omega) &= \frac{1}{2\pi}\int_{-\infty}^{\infty}\int e^{i(Qr-\omega t)}G_s(r,t)drdt, \end{aligned} \tag{2.8}$$

where the scattering functions S and S_s are related to the coherent and incoherent cross sections in equation 2.6 by equation 2.1 and 2.3 as

$$\begin{aligned}(\frac{d^2\sigma}{dE'd\mu})_{coh} &= \frac{\sigma_{coh}}{4\pi\hbar}\sqrt{\frac{E}{E'}}S(Q,\omega),\\ (\frac{d^2\sigma}{dE'd\mu})_{incoh} &= \frac{\sigma_{incoh}}{4\pi\hbar}\sqrt{\frac{E}{E'}}S_s(Q,\omega).\end{aligned} \tag{2.9}$$

Note here that the coherent cross section contains both the distinct and the self dynamics. Equation 2.6 gives the total differential cross section as a sum of the coherent and incoherent parts. With equations 2.7, 2.8 and 2.9 an alternative notation for the total differential cross section, which separates the distinct and self dynamics, is given as

$$\frac{d^2\sigma}{dE'd\mu} = \frac{1}{4\pi\hbar}\sqrt{\frac{E}{E'}}(\sigma_{coh}S_d(Q,\omega) + (\sigma_{coh}+\sigma_{incoh})S_s(Q,\omega)). \tag{2.10}$$

The constants σ_{coh} and σ_{incoh} correspond to the respective bound scattering cross sections, with the total σ_b given by

$$\sigma_b = \sigma_{coh} + \sigma_{incoh}. \tag{2.11}$$

The bound scattering cross sections contain the nuclear aspects of the scattering, i.e. the interaction between the neutron and the nucleus, while S and G contain the dynamics of the scattering system and interactions between the scattering atoms. The bound scattering cross section is used to calculate two parameters that are given as inputs in LEAPR. The first parameter is the free atom scattering cross section, σ_f, which is given in the input variable *spr*. It is calculated from the σ_b as

$$\sigma_f = \sigma_b\frac{A}{A+1}, \tag{2.12}$$

where A is the mass number of the scatterer. For hydrogen $A = 1$ and the equation simply becomes

$$\sigma_f = \frac{\sigma_b}{4}.$$

The other input parameter is the coherent fraction, given in the variable $cfrac$. The coherent fraction gives the weight of the coherent scattering and is calculated as

$$cfrac = \frac{\sigma_{coh}}{\sigma_b}.$$

2.2 Neutron scattering in para-hydrogen

The nucleus of a hydrogen atom consists of a single proton with spin $s = 1/2$. The nuclei in an H_2 molecule can then form states of total spin $S = 0$ or

$S = 1$, depending on if the spins are anti-parallel ($S = 0$) or parallel ($S = 1$). The molecules in the $S = 0$ state are called para-hydrogen and the ones in the $S = 1$ state are called ortho-hydrogen. This spin correlation must be taken into account when evaluating the total differential cross section for liquid hydrogen. Following the work of Young and Koppel [16] and Guarini et al. [8, 17], an approach to calculating the thermal scattering law and the double differential cross section, that is valid for liquid hydrogen, is presented below. The calculations done by Young and Koppel [16], and Guarini et al. [17], take into account the spin correlation as well as the possible transitions between an initial and final vibrational, rotational and translational state of the hydrogen molecule.

It is shown by Guarini et al. [8] that the total differential scattering cross section for para-hydrogen can be written in a similar way to equation 2.10, dividing the problem into it's self and distinct dynamics,

$$\begin{aligned}\frac{d^2\sigma}{dE'd\mu} =& \sqrt{\frac{E}{E'}}(u(Q)S_{d,c.m.}(Q,\omega)+ \\ & \sum_{J_0 J_1 v_0 v_1} F_{J_0 J_1 v_0 v_1}(Q) S_{s,c.m.}(Q, E - E_{J_0 J_1} - E_{v_0 v_1}).\end{aligned} \tag{2.13}$$

The differences here to equation 2.10 is partly the introduction of the subscript c.m. which indicates that the distinct and self dynamics considered here are the dynamics of the centre of mass of the hydrogen molecules. In this notation, the c.m. dynamics contain the translational modes while the sum in the second part of equation 2.13 then represents the convolution of the c.m. self dynamics with the possible rotational and vibrational transitions of the molecule. Here J_0 and J_1 are the initial and final rotational states and v_0 and v_1 are the initial and final vibrational states. $u(Q)$ and $F_{J_0 J_1 v_0 v_1}(Q)$ are Q-dependent weight functions containing the bound scattering cross section and are given in detail in [17].

The inelastic scattering for liquid para-hydrogen is mostly incoherent [10] and is sufficiently described by the self-dynamics. However, at low incident neutron energies (on the order of 3.5 meV, as seen in equation 2.5), coherent scattering effects must also be taken into account. The problem is that the distinct pair distribution function, G_d, typically is a complicated function. Instead of calculating it explicitly, an approximation was developed by Vineyard [14] and later improved by Sköld [15], which uses a modification of the self part of the scattering law to model the coherent scattering law. The Vineyard approximation is given by

$$S_{c.m.}(Q,\omega) = S(Q) S_{s,c.m.}(Q,\omega), \tag{2.14}$$

while the Sköld approximation is slightly altered as

$$S_{c.m.}(Q,\omega) = S(Q)S_{s,c.m.}(\frac{Q}{\sqrt{S(Q)}},\omega). \tag{2.15}$$

The function $S(Q)$ used in both approximations is called the static structure factor and contains information about the correlations of the positions of nearby molecules. The static structure factor can be determined by experimental data [8], however, it can also be calculated from molecular dynamics results. The detailed description on how to compute $S(Q)$ from molecular dynamics is given in Chapter 3. Within the Skold approximation, an expression can then be found for the distinct part of the scattering law used in equation 2.13 as

$$S_{d,c.m}(Q,\omega) = S(Q)S_{s,c.m.}(\frac{Q}{\sqrt{S(Q)}},\omega) - S_{s,c.m.}(Q,\omega). \tag{2.16}$$

The H2D2-model of NJOY [4,5] implements the Sköld approximation in a similar way. Namely, using the c.m. self dynamics instead of the total self dynamics including the rotational modes [6], as previous versions of NJOY had done.

In the following subsections, the c.m. and total self dynamics will be evaluated in more detail, as implemented in NJOY.

2.2.1 Rotational- and vibrational modes

Young and Koppel [16] make the assumption that the translational modes can be separated from the rest of the self dynamics. In the following discussions the notations are changed to describe the TSL in terms of α and β, and $S_t(\alpha,\beta)$ is used to denote the c.m. dynamics since it contains the translational modes. The total self part of the TSL can then be written as a convolution of $S_t(\alpha,\beta)$ and a function $S_{S,J,v}(\alpha)$ containing the rotational, vibrational and spin-dependent effects,

$$S_s(\alpha,\beta) = S_t(\alpha,\beta) \times S_{S,J,v}(\alpha). \tag{2.17}$$

They further assume the molecular Hamiltonian to be spin-independent and the coupling between rotation and vibration is neglected. The rotational energy levels of a diatomic molecule with fixed bond length, a, are given by

$$E_J = \frac{\hbar^2 J(J+1)}{4ma^2} = 0.015\frac{J(J+1)}{2}\text{eV}, \tag{2.18}$$

where J is the total angular momentum quantum number. Since $S = 0$ for para-hydrogen, only rotational states of even J are allowed (J=0,2,4...). For ortho-hydrogen only odd J are allowed. The vibrations in the hydrogen molecule are described as the two atoms vibrating around their separation distance, a, and is

assumed to behave like a harmonic oscillator. The energy levels for a harmonic oscillator are given by

$$E_n = (n + \frac{1}{2})\hbar\omega_v, \tag{2.19}$$

where n is the vibrational quantum number and ω_v is the angular frequency of the oscillator. For a hydrogen molecule, $\hbar\omega_v = 0.546$ eV and the lowest vibrational transition in para-hydrogen is therefore at $E = 0.546$ eV above the vibrational ground state. The average molecular kinetic energy is related to the temperature as

$$\langle E_k \rangle = \frac{2}{3} k_b T.$$

For a temperature of $T = 20$ K, the average molecular energy is $\langle E_k \rangle = 0.001$ eV and all the hydrogen molecules can be assumed to be in their rotational and vibrational ground states. If the incoming neutrons have high enough energy, they can introduce transitions to the higher states. If only the scattering of neutrons of initial energies 'sufficiently less' [16] than 0.546 eV is considered, such that the vibrational transitions need not be considered, then the function $S_{S,J,v}(\alpha)$ can be written as

$$\begin{aligned} S_{S,J,v}(\alpha) = \sum_{J=0,2,4..} P_J \frac{4\pi}{\sigma_b} (a_c^2 \sum_{J'=0,2,4...} + a_i^2 \sum_{J'=1,3,5...}) \\ \times (2J'+1) \sum_{l=|J'-J|}^{J'+J} 4 j_l^2(y) C^2(JJ'l:00). \end{aligned} \tag{2.20}$$

Here P_J is a statistical weight vector, a_c and a_i are the coherent and incoherent scattering lengths, connected to the bound scattering cross section, σ_b, by

$$\sigma_b = 4\pi(a_c^2 + a_i^2),$$

$j_l(x)$ is a spherical Bessel function of order l and $C^2(JJ'l:00)$ is a Clebsch-Gordan coefficient. y is given by

$$y = \frac{a}{2}\sqrt{4mk_bT\alpha/2},$$

where α is the dimensionless momentum transfer from equation 2.2. The sums in equation 2.20 are written as operators so that the equation is more compact.

2.2.2 Translational modes

To calculate the translational part, S_t, Young and Koppel [16] assume that the molecular translations are free, which is a good assumption for hydrogen gas. However, for liquid hydrogen this assumption is no longer correct as the molecules in the liquid interact with each other. A model by Keinert and Sax [18]

models the collective translational modes of a liquid as a combination of a solid-like phonon distribution and a diffusion component. The idea is that solid-like clumps of hydrogen molecules diffuse through a liquid [3]. In a solid crystal structure, an incoming neutron can excite vibrations, or phonons, of the whole crystal. The phonon distribution, $\rho(\omega)$, or frequency spectrum, then describes the probability of a vibration with a frequency, ω. In order to keep the notations in this section consistent with the NJOY manual [3], the frequency is denoted by the dimensionless β defined in equation 2.4. In the Keinert and Sax model [18], the effective phonon distribution, $\rho_{tot}(\beta)$ is described by a combined solid part and a diffusion component,

$$\rho_{tot}(\beta) = \rho_{solid}(\beta) + \rho_{diff}(\beta). \tag{2.21}$$

Solid component

For a phonon distribution from a solid crystal, $\rho_{solid}(\beta)$, the theory of calculating the thermal scattering law is well explained in for example Bell and Glasstone [10]. Applying the theory from Bell and Glasstone, and as described in the NJOY manual [3], the translational part of the thermal scattering law, $S_t(\alpha, \beta)$, can be calculated from $\rho_{solid}(\beta)$ with the Gaussian approximation,

$$S_t(\alpha, \beta) = \frac{1}{2\pi} \int_{-\infty}^{\infty} e^{i\beta t} e^{-\alpha\gamma(t)} dt, \tag{2.22}$$

with the function $\gamma_1(t)$ given by

$$\gamma(t) = \int_{-\infty}^{\infty} \frac{\rho_{solid}(\beta)}{2\beta \sinh(\beta/2)} (1 - e^{-i\beta t}) e^{-\beta/2} d\beta. \tag{2.23}$$

The diffusion part of the phonon distribution typically decreases to zero relatively fast. However, the solid-like part does not necessarily do so, which causes the integration in equation 2.23 to be computationally heavy. To simplify the calculations, in the LEAPR module in NJOY, the Gaussian approximation in equation 2.22 is decomposed and the solid-like and diffusion parts of S_t are calculated separately and then convoluted together. To simplify the calculation of the integral, the exponential $e^{\gamma(t)}$ is expanded in time in a phonon expansion,

$$e^{-\alpha\gamma(t)} = e^{-\alpha\lambda} \sum_{n=0}^{\infty} \frac{1}{n!} (\alpha \int_{-\infty}^{\infty} \frac{\rho_{solid}(\beta)}{2\beta \sinh(\beta/2)} e^{-i\beta t} e^{-\beta/2} d\beta)^n, \tag{2.24}$$

where

$$\lambda = \int_{-\infty}^{\infty} \frac{\rho_{solid}(\beta)}{2\beta \sinh(\beta/2)} e^{-\beta/2} d\beta. \tag{2.25}$$

With this, the solid part of the translational TSL can be written as

$$S_{t,solid}(\alpha,\beta) = e^{-\alpha\lambda}\sum_{n=0}^{\infty}\frac{1}{n!}\alpha^n\frac{1}{2\pi}\int_{-\infty}^{\infty}e^{i\beta t} \left(\int_{-\infty}^{\infty}\frac{\rho_{solid}(\beta')}{2\beta'\sinh(\beta'/2)}e^{-i\beta' t}e^{-\beta'/2}d\beta'\right)^n dt. \tag{2.26}$$

This phonon expansion requires that the solid-like frequency spectrum behaves like β^2 when $\beta \to 0$ [3, 20].

Diffusion component

The diffusion component in equation 2.21 is given by the Egelstaff and Schofield diffusion model [19] as

$$\rho_{diff}(\beta) = \frac{4pw_t}{\pi}\sqrt{p^2+0.25}\sinh\left(\frac{\beta}{2}\right)K_1(\beta\sqrt{p^2+0.25}), \tag{2.27}$$

where w_t is the weight of the diffusion component, $K_1(x)$ is the modified Bessel function of the second kind and

$$p = \frac{mD}{w_t\hbar}$$

is a dimensionless diffusion coefficient. D is the diffusion constant and can be determined from experiment, or it can be calculated from molecular dynamics results, as will be discussed in Chapter 3.

With this, it is shown [3] that the diffusion part of the translational TSL can be written as

$$S_{t,diff}(\alpha,\beta) = \frac{2pw_t\alpha}{\pi}e^{2p^2w_t\alpha-\beta/2}\frac{\sqrt{p^2+0.25}}{\sqrt{\beta^2+4p^2w_t^2\alpha^2}} K_1(\sqrt{p^2+0.25}\sqrt{\beta^2+4p^2w_t^2\alpha^2}). \tag{2.28}$$

2.2.3 Total self dynamics

The solid- and diffusion parts in equations 2.26 and 2.28 are then convoluted together,

$$S_t = S_{t,solid} \times S_{t,diff}, \tag{2.29}$$

and the total self part of the TSL is given by equations 2.17 and 2.20 as [3]

$$\begin{aligned} S_s(\alpha,\beta) = \sum_{J=0,2,4..} P_J \frac{4\pi}{\sigma_b}(a_c^2 \sum_{J'=0,2,4...} + a_i^2 \sum_{J'=1,3,5...}) \\ \times S_t(w_f\alpha, \beta + \beta_{J,J'}) \\ \times (2J'+1) \sum_{l=|J'-J|}^{J'+J} 4j_l^2(y) C^2(JJ'l:00). \end{aligned} \tag{2.30}$$

w_f is here the translational weight factor, which for a hydrogen molecule is 0.5 and

$$\beta_{J,J'} = \frac{E_{J'} - E_J}{k_b T}$$

is the energy transfer for a rotational transition.

2.2.4 Translational modes from molecular dynamics

A new method to simulate the translational dynamics using molecular dynamics has been used by e.g. Márquez Damián et al. [7] to compute the scattering law for water. They use molecular dynamics to compute a frequency spectrum to use in the Gaussian approximation instead of the solid-like phonon distribution. A detailed description of how to compute the frequency spectrum from molecular dynamics is given in Chapter 3. The molecular dynamics simulations capture the full translational dynamics of the scattering medium, including diffusion. Since the diffusion and solid parts are decoupled in LEAPR, a diffusion component calculated according to the Egelstaff and Schofield model in equation 2.27 is subtracted from the full frequency spectrum in order to get a component to replace the solid-like frequency spectrum in the input to LEAPR. This is because the LEAPR module is not suited for taking the full translational frequency spectrum as an input, and an equal diffusion part is subtracted as the diffusion part added in NJOY. As such, the resulting scattering law should correspond to one that is calculated from the full frequency spectrum. A future possible upgrade to LEAPR is to instead take the full translational frequency spectrum as input, avoiding the need to subtract a diffusion component.

Liquid hydrogen is a quantum liquid, and as such regular molecular dynamics is not sufficient to model its dynamics. A similar method using quantum molecular dynamics has been used by e.g. Guarini et al. [8] and Miller and Manolopoulos [9] to calculate the frequency spectrum for liquid hydrogen. This method was used in the present project and is described in detail in Chapter 3. Guarini et al. [8] also calculate the total cross section directly from the molecular dynamics results using the Gaussian approximation as well as the formalism of Young and Koppel [16]. While this method avoids the approximation of the phonon

expansion used in NJOY, for this project it is deemed too computationally heavy. Instead, an attempt was made to incorporate the quantum molecular dynamics used by Guarini et al. [8] and Miller and Manolopoulos [9] into the method suggested by Márquez Damián et al. [7], using the standard tool for calculating scattering kernels, NJOY.

Chapter 3

Molecular dynamics

Molecular dynamics (MD) is a popular method to model a material to gain information about its structure and dynamics on an atomic scale. The basic idea behind MD is simple: A small scale sample of the material is initiated by setting the positions and initial velocities of each atom, as well as the potential with which the atoms interact with each other. The sample is then allowed to evolve over a series of time steps, where in each step the total forces on the atoms are calculated and Newton's equations are solved to determine the movement of the atoms. Global properties of the system such as pressure and temperature can then be calculated from the motions of the atoms.

3.1 Interatomic potential

The choice of interatomic potential in the MD simulation is of importance since it will govern the interaction between the atoms and as such, the dynamics of the system as whole. For liquid para-hydrogen, a common choice of this potential is the Silvera-Goldman potential [8, 9, 21], in which the interacting hydrogen molecules are treated as sphere particles. This treatment is valid when the hydrogen molecules are in their rotational ground state [21], which they are at the low temperatures considered in the present report. The Silvera-Goldman potential is given by

$$V(r) = e^{\alpha_c - \beta_c r - \gamma_c r^2} - (\frac{C_6}{r^6} + \frac{C_8}{r^8} - \frac{C_9}{r^9} + \frac{C_{10}}{r^{10}}) f_c(r), \tag{3.1}$$

where r is the distance between the spheres and

$$f_c(r) = e^{-(r_c/r-1)^2}$$

if $r \leq r_c$ and $f_c(r) = 1$ otherwise. The values used for the parameters are given in table 3.1.

α_c	1.713	C_6	12.14
β_c	1.5671	C_8	215.2
γ_c	0.00993	C_9	143.1
r_c	8.32	C_{10}	4812.9

Table 3.1: Parameters used in the Silvera-Goldman potential in equation 3.1. All parameters are given in atomic units.

3.2 Initial configuration

To initiate the MD simulation, the density of the material is set by stating the number of particles to simulate as well as the volume of a simulation box, containing all the particles. The simulation box can be set to have periodic boundary conditions, where a particle flying out of the box on one side will reappear on the opposite side with the same velocity vector. In this way a small simulation box can be approximated as a piece of a larger, interacting system. Furthermore, the initial positions and velocities of the particles must be set before starting the simulation. For a solid in a known crystal structure, the initial positions of the particles are set to match the crystal structure. For a liquid, in contrast, the real positions of the molecules are randomly distributed throughout the volume. However, to initiate a MD system with randomly distributed particles can be problematic, as there is a chance that two particles will be initiated right on top of each other. Then when the interactions are calculated in the first time step, the force between the particles will blow up. This is problematic for two reasons. The first reason is that the total energy of the system is conserved in the MD simulation, so if the initial system has a very high potential energy, as time progresses, the kinetic energy of the system will be increased, and since the kinetic energy of the system increasing, so will the temperature. The second reason is that if the forces calculated in the first time step are too large, the simulation might 'lose particles' as their velocities become too large for the simulation to handle. The typical way to simulate a liquid system is instead to initiate the particles in a solid-like, cubic crystal structure, and let the system 'melt' into a liquid state. The initial velocities of the particles will give the total kinetic energy of the system which is related to the temperature of the system. A common way to set the initial velocities is therefore to sample the velocities randomly from a Maxwell-Boltzmann distribution at the desired initial temperature [22].

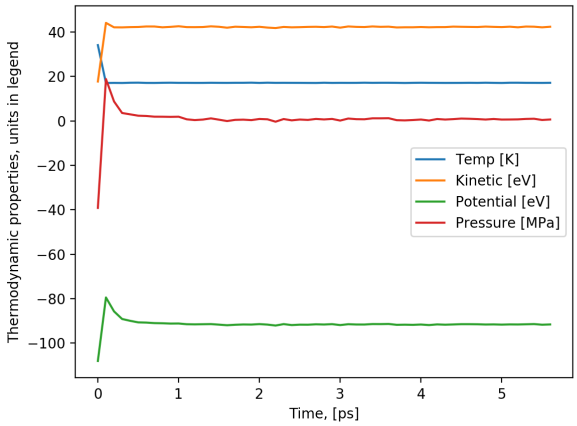

Figure 3.1: Results from a typical equilibrium run. The calculated quantities have been printed out from the simulation at each 1000th time step and are plotted in the figure. The units of the quantities are chosen as to fit all graphs in the same figure.

3.3 Equilibrium run

When the system is initialised, the initial values are given for the positions and velocities of the particles. In general, this initial state will not be in equilibrium and there will be a drift in the calculated average quantities such as the potential and kinetic energy, pressure and temperature of the system. Because of this, the system has to go through an equilibrium simulation run for a number of time steps until these average quantities stabilize. Typical results from such an equilibrium run are seen in figure 3.1, where the potential and kinetic energies, pressure and temperature of the system are plotted against the time of the simulation. The quantities experience a drift from their initial values for the first few time steps, after which they settle around an average value. There will still be some fluctuations around this average value as the simulation progress, however it is the average value that is considered constant in the system.

MD simulations are often carried out in the micro-canonical ensemble (NVE), in which the number of particles (N), the volume (V) and the total energy (E) are conserved in each time step. Often, however, a system is specified not by the total energy but by the temperature. Trouble may then arise, as discussed earlier, if the initial conditions are not set perfectly and the initial potential energy due to the positions of the particles is too high or low. This will then

carry over to the kinetic energy and hence the temperature of the system will drift away from the intended value. A way to circumvent this problem is to run the system through an equilibrium run in a canonical (NVT) ensemble, in which the number of particles, volume and temperature (T) are conserved, instead of the total energy. This is done by using a thermostat, introducing a new degree of freedom of the system that represents an interaction with a larger system. The larger system can then exchange excess energy with the simulated system in order to keep the temperature constant [22]. As an example, a common type of thermostat is the Langevin thermostat, in which the particles in the system are considered moving through a continuum of smaller particles. The smaller particles then create a damping force, or 'drag', on the bigger particles as the bigger particles move through the smaller ones, pushing them out of the way. The smaller particles also have thermal (kinetic) energy and will give random 'kicks' to the bigger particles. The Langevin equation is then a modification to the Newton equation [22] ,

$$m\frac{d^2\vec{r}}{dt^2} = \vec{F} - \gamma\frac{d\vec{r}}{dt} + \vec{F}_{rand}(t), \tag{3.2}$$

where $\vec{F}$ is the normal interatomic force term, $F = -\boldsymbol{\nabla}\cdot V$, with the interatomic potential V, γ is the drag coefficient and $\vec{F}_{rand}(t)$ is the force term from the random kicks from the thermal motion of the small particles, usually referred to as noise. The damping force and the random force combined puts the system in the canonical ensemble.

3.4 Trajectory run

After the system is equilibrated, the system is moved over to the micro-canonical ensemble, keeping the energy of the system constant, and the trajectories of the particles are collected in order to calculate the velocity auto-correlation function. This is typically done a number of times and an average is taken in order to get a statistically reliable result.

3.5 Calculating the static structure factor

The static structure factor, $S(Q)$, is given as an input for LEAPR as it is needed in the implementation of the Sköld and Vinyard approximations. The static structure factor can be determined by neutron scattering experiments, see for example [23, 24], but it can also be calculated from the radial distribution function, $g(r)$, through the Fourier transform

$$S(Q) = 1 + \frac{4\pi\rho}{Q}\int_0^\infty r\sin(Qr)h(r)dr, \tag{3.3}$$

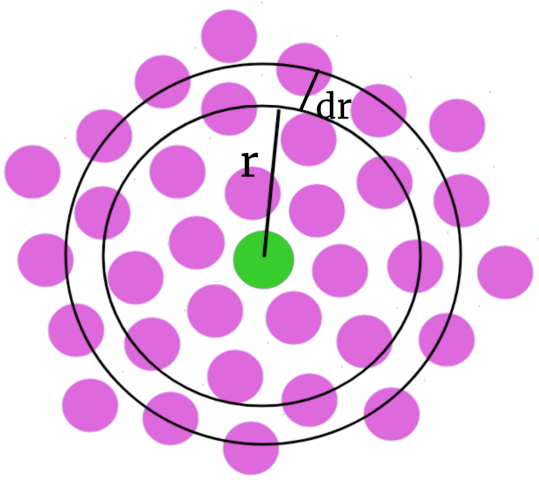

Figure 3.2: Simple sketch to illustrate the radial distribution function. At each distance r from the centre of the particle, the number of surrounding particles with their centres at a distance $r + dr$ is counted.

where $h(r) = g(r) - 1$ and ρ is the density. The radial distribution function describes the probability of, from a certain particle, finding another particle at a distance r from the first particle. It therefore gives information about the structure of a material. For a gas this function is expected to be constant, related to the density of the gas, while for a solid in a crystal structure for example, it is expected to have a clear pattern in the radial distribution function, related to the structure of the crystal lattice. For a liquid the radial distribution function is expected to show some structure for short distances, r, as the particles will bundle together somewhat uniformly around each other, as is illustrated in figure 3.2. However at larger distances, the function will average out to the density of the liquid.

In a homogeneous and isotropic system of N particles, $g(r)$ is calculated as

$$g(r) = \frac{\langle \sum_{i \neq j}^{N} \delta(r - |\vec{r_i} - \vec{r_j}|) \rangle}{\rho}, \tag{3.4}$$

where $\vec{r}$ gives the position vector of the particle and $\langle ... \rangle$ indicates the average [11]. The function is normalised by the density so that it converges to one for large distances r. The radial distribution function can be calculated from the output trajectories of a molecular dynamics simulation. In practice, the

calculations of equation 3.4 are done by looping over all the particles, and for each creating a histogram containing how many other particles are found within a spherical slice with radius $r + dr$ from the particle. The histograms are then summed together and normalised by the number of particles, the density and the volume of the slices. The range of the radial distribution function calculated from a molecular dynamics simulation is fundamentally limited by the dimensions of the simulation box. However, for the integral in equation 3.3 to fully converge, often $g(r)$ must be extrapolated smoothly to larger r values. This is done with the function

$$h(r) = \frac{A_0}{r} e^{-\frac{r}{r_0}} \sin\left(\frac{r}{r_1}\right), \tag{3.5}$$

in which the parameters A_0, r_0 and r_1 are found by fitting the function to the calculated $g(r) - 1$ from around the third zero [23].

3.6 The velocity auto-correlation function

The velocity auto-correlation function, $u(t)$ or VACF, describes how the velocity of a particle in a material at a time $t_0 + t$ is correlated to its velocity at the time t_0. It is calculated according to equation 3.6 [22] where the velocity of the i-th atom is denoted as $\vec{v}_i$ and the brackets indicate the average over N atoms and over a number of initial times, t_0.

$$u(t) = \langle \vec{v}_i(t + t_0) \cdot \vec{v}_i(t_0) \rangle = \sum_{t_0} \sum_{i=0}^{N-1} \vec{v}_i(t + t_0) \cdot \vec{v}_i(t_0) \tag{3.6}$$

For $t = 0$ the VACF can be written in terms of the scalar velocity, v, as

$$\langle \vec{v}_i(t_0) \cdot \vec{v}_i(t_0) \rangle = \langle v^2 \rangle,$$

where $\langle v^2 \rangle$ is related to the average kinetic energy, $\langle K \rangle$, and hence the temperature, T, by

$$\langle K \rangle = m\langle v^2 \rangle / 2 = 3k_b T/2$$

or

$$\langle v^2 \rangle = 3k_b T/m.$$

In the limit case of $t \to \infty$ it will, for a gas, be equal to 0 as there is no correlation between velocities in a gas in thermal equilibrium and no flow. In a gas the atoms collide with each other with typical collision times τ and at each collision the single atom will 'forget' its initial velocity. The VACF for a gas is therefore expected to decay exponentially to 0 with the exponential constant $\frac{1}{\tau}$. In a solid material, the atoms are vibrating around an equilibrium position and therefore its VACF will be given by a superposition of sinusoidal curves

with eigenfrequencies corresponding to the atoms' phonons. A liquid can be seen as a middle way between a gas and a solid, with the VACF showing some phonon curves before diffusing out to 0. The frequency distribution, $\rho(\omega)$, gives information about the translational motion of the atoms and is given by the Fourier transform of the VACF as

$$\rho(\omega) = \frac{1}{2\pi} \int_{-\infty}^{\infty} u(t) e^{-i\omega t} dt. \tag{3.7}$$

3.7 Quantum molecular dynamics

In some cases such as liquid hydrogen, when quantum mechanical effects should be taken into account, a modification to the classical MD is needed to simulate the system. Such modifications, called quantum molecular dynamics (QMD), have been developed that use different methods to take into account the quantum mechanical effects. One QMD method is the path integral molecular dynamics (PIMD) in which the nucleus of each atom is replaced by a number of fictional "beads" connected by springs forming a polymer ring. The Hamiltonian of the nucleus is then derived from the Feynman path integral of the beads.

3.7.1 Path integral molecular dynamics

The following derivations of the path integral molecular dynamics formalism are based on [25]. The path integral is a method used to describe a process in which a particle moves unobserved between an initial positional state, $|x\rangle$, and a final state, $|x'\rangle$. (The initial and final states are here written in the bra-ket notation). The exact path the particle takes between the two states is unknown, but the amplitude, or probability of finding the particle in the second state can be calculated as the integral over the possible paths it could have taken. The amplitude, A, is given by

$$A = \langle x' | \, e^{-i\hat{H}t/\hbar} \, | x \rangle \, , \tag{3.8}$$

where $e^{-i\hat{H}t/\hbar}$ is the propagator with $\hat{H}$ being the Hamiltonian operator. A general state vector at time t, $|\Psi(t)\rangle$, is given by the propagator acting on the initial state $|\Psi(0)\rangle$. Projecting this into the positional basis, with the completeness relation over the states $|x\rangle$,

$$I = \int |x\rangle \langle x| \, dx, \tag{3.9}$$

the general state at time t and position x', $\Psi(x', t)$, is given by

$$\begin{aligned}\Psi(x',t) &= \langle x'|\Psi(t)\rangle = \langle x'|\, e^{-i\hat{H}t/\hbar}\,|\Psi(0)\rangle \\ &= \int dx\, \langle x'|\, e^{-i\hat{H}t/\hbar}\,|x\rangle\, \langle x|\Psi(0)\rangle \\ &= \int dx A\Psi(x,0).\end{aligned} \tag{3.10}$$

The Hamiltonian operator $\hat{H}$ is the sum of the kinetic energy operator, $\hat{T}$, and the potential energy operator, $\hat{U}$, as $\hat{H} = \hat{T} + \hat{U}$. The operators $\hat{T}$ and $\hat{U}$ do generally not commute but according to the Trotter theorem [25], the following relation holds,

$$e^{-\beta_i H} = e^{-\beta_i(\hat{T}+\hat{U})} = \lim_{P\to\infty}(e^{-\frac{\beta_i}{2P}\hat{U}}e^{-\frac{\beta_i}{P}\hat{T}}e^{-\frac{\beta_i}{2P}\hat{U}})^P. \tag{3.11}$$

With this, and with the variable change, $t = -i\beta_i\hbar$, equation 3.8 is written as

$$A = \lim_{P\to\infty}\langle x'|\,(e^{-\frac{\beta_i}{2P}\hat{U}}e^{-\frac{\beta_i}{P}\hat{T}}e^{-\frac{\beta_i}{2P}\hat{U}})^P\,|x\rangle\, dx = \lim_{P\to\infty}\langle x'|\,\Omega^P\,|x\rangle\,, \tag{3.12}$$

where the variable,

$$\Omega = e^{-\frac{\beta_i}{2P}\hat{U}}e^{-\frac{\beta_i}{P}\hat{T}}e^{-\frac{\beta_i}{2P}\hat{U}},$$

has been introduced to simplify. Now if the completeness relation from equation 3.9 is inserted between each factor Ω and denoting each set x by x_n with $n = 2...P$, equation 3.12 becomes

$$\begin{aligned}A &= \lim_{P\to\infty}\langle x'|\,\Omega^P\,|x\rangle \\ &= \lim_{P\to\infty}\int \langle x'|\,\Omega\,|x_2\rangle\,\langle x_2|\,\Omega\,|x_3\rangle\,...\,\langle x_P|\,\Omega\,|x\rangle\, dx_2dx_3...dx_P.\end{aligned} \tag{3.13}$$

Now, considering each of the matrix elements, written in a general way as

$$\langle x_k|\,\Omega\,|x_{k+1}\rangle = \langle x_k|\,e^{-\frac{\beta}{2P}\hat{U}}e^{-\frac{\beta_i}{P}\hat{T}}e^{-\frac{\beta_i}{2P}\hat{U}}\,|x_{k+1}\rangle\,. \tag{3.14}$$

The potential operator $\hat{U} = U(\hat{x})$ is a function of the position operator and the position eigenvectors $|x_k\rangle$ are then also eigenvectors of $e^{-\frac{\beta_i}{2P}\hat{U}}$ with eigenvalues $e^{-\frac{\beta_i}{2P}U(x_k)}$. The matrix elements can then be simplified as

$$\langle x_k|\,\Omega\,|x_{k+1}\rangle = e^{-\frac{\beta_i}{2P}U(x_k)}\,\langle x_k|\,e^{-\frac{\beta_i}{P}\hat{T}}\,|x_{k+1}\rangle\,e^{-\frac{\beta_i}{2P}U(k_{k+1})}. \tag{3.15}$$

To evaluate the kinetic operator, a complete set of momentum eigenstates, $|p\rangle$, is introduced and the completeness relation

$$I = \int |p\rangle\,\langle p|\,dp, \tag{3.16}$$

is inserted in the kinetic part of equation 3.15, which can then be written as

$$\langle x_k|\, e^{-\frac{\beta_i}{P}\hat{T}}\, |x_{k+1}\rangle = \int dp\, \langle x_k|\, e^{-\frac{\beta_i}{P}\hat{T}}\, |p\rangle\, \langle p|x_{k+1}\rangle\,. \tag{3.17}$$

The kinetic operator now acts on the momentum eigenvector to yield the eigenstate $e^{-\frac{\beta_i p^2}{2mP}}$ and since

$$\langle x|p\rangle = \frac{1}{\sqrt{2\pi\hbar}} e^{\frac{ipx}{\hbar}}$$

[25], equation 3.17 can be written as

$$\langle x_k|\, e^{-\frac{\beta_i}{P}\hat{T}}\, |x_{k+1}\rangle = \frac{1}{2\pi\hbar}\int dp e^{-\frac{\beta_i p^2}{2mP}} e^{\frac{ip(x_k - x_{k+1})}{\hbar}}. \tag{3.18}$$

The integral in equation 3.18 is a Gaussian integral and is evaluated in [25]. Using their result and multiplying all P matrix elements from equation 3.13 together, the amplitude is given by

$$A = \lim_{P\to\infty} (\frac{mP}{2\pi\beta_i\hbar^2})^{P/2} \int dx_2 ... dx_P \\ e^{-\frac{1}{\hbar}\sum_{k=1}^{P}(\frac{mP}{2\beta_i\hbar}(x_k - x_{k+1})^2 + \frac{\beta_i\hbar}{2P}(U(x_k)+U(x_{k+1})))}, \tag{3.19}$$

where $x_1 = x$ and $x_{P+1} = x'$. The amplitude describes the propagation of a particle between an initial state, x, and a final state x'. The integration over each x_i in equation 3.19 can then be interpreted as the summing of all the possible paths the propagation can take. If the particle is confined to a certain interval, $x \in [0, L]$, the integrations will also be restricted to this interval. The canonical partition function, $Z(L,T)$, can be used to describe a system in thermodynamic equilibrium. It is calculated as

$$Z(L,T) = \int_0^L dx\, \langle x|\, e^{-\beta_i \hat{H}}\, |x\rangle\,, \tag{3.20}$$

which can be calculated by equation 3.19 by setting $x_1 = x_{P+1} = x$. This restricts the integrations to paths that begin and end in the same point. If the limit is removed from equation 3.19 in order to consider a finite number P, it is shown in [25] that the partition function for finite P, $Z_P(L,T)$, can be written as

$$Z_P(L,T) = (\frac{mP}{2\pi\beta_i\hbar^2})^{P/2} \int_0^L dx_2 ... dx_P \\ e^{-\frac{1}{\hbar}\sum_{k=1}^{P}(\frac{mP}{2\beta_i\hbar}(x_k - x_{k+1})^2 + \frac{\beta_i\hbar}{P}(U(x_k)))}. \tag{3.21}$$

It is further shown that equation 3.21 can be modified to resemble the canonical partition function of a cyclic polymer chain of P beads, moving in a classical

potential $U(x)/P$. This is done by replacing the factor $(\frac{mP}{2\pi\beta_i\hbar^2})^{P/2}$ by a set of Gaussian integrals over variables $p_1, ..., p_P$, which are introduced to resemble the momentum. The modified expression is given by

$$Z_P(L,T) = \int dp_1...dp_P \int_0^L dx_2...dx_P \; e^{-\beta_i \sum_{k=1}^{P} (\frac{p_i^2}{2m'} + \frac{m\omega_P^2}{2}(x_k - x_{k+1})^2 + \frac{1}{P}(U(x_k)))}, \tag{3.22}$$

where variable m' is introduced and is given by

$$m' = \frac{mP}{(2\pi\hbar)^2}.$$

However, it is shown that this factor does not affect any of the thermodynamic averages and can be set as a free parameter. The frequency ω_P is also introduced, given by

$$\omega_P = \frac{\sqrt{P}}{\beta_i\hbar}.$$

This frequency is interpreted as the frequency of the harmonic coupling between the closest neighbours in the cyclic chain. With this result, the partition function for a finite number P is found to be equal to that of a classical polymer chain of P beads, moving in a potential, $U(x)/P$, and connected with each other by springs with spring constants, $k = m\omega_P^2$. Note that this is an approximation of the system, and that the exact quantum partition function is found in the limit $P \to \infty$. The validity of the approximation is in other words dependent on the number of beads, P, which is also referred to as the Trotter number, due to it's origin from the Trotter theorem.

The polymer chains propagate in imaginary time, $\beta_i = it\hbar$, and it can be shown that in a system with many interacting particles, each being represented by a polymer chain, that the individual beads only interact with corresponding beads with the same imaginary time index, k [25]. This is illustrated in figure 3.3. In this way a system of N quantum particles can be simulated as P parallel systems, each with N classical particles, where the systems are connected by springs. The velocity auto-correlation is related to the the partition function and while it is possible to compute it directly from the PIMD formalism, the method is numerically difficult. To simplify the calculations of the correlation functions, two approximate variants of the PIMD method commonly used are centroid molecular dynamics (CMD) and ring-polymer molecular dynamics (RPMD) [25]. The main differences between the methods lie in the masses used for the beads and the use of thermostats [26]. In RPMD the masses for the beads are taken as the real masses of the particles, $m' = m$. Studies have been made to compare the methods. For example, Hone, et al. [21] showed that

CMD compared slightly better to the results from the PIMD than RPMD when calculating the kinetic energy for para-hydrogen at 14 K. When comparing the VACF and frequency spectrum, results of importance for this study, the difference between the methods is almost not noticeable. Furthermore, RPMD is less computationally demanding than CMD [21]. In the present work, the RPMD method was used.

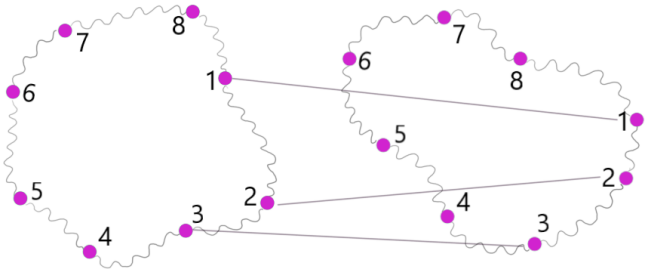

Figure 3.3: Simple sketch to illustrate two interacting polymer chains. Only beads with the same index interact with each other.

3.7.2 Canonical velocity auto-correlation function

From RPMD the Kubo-transformed, or canonical, velocity auto-correlation function, $u_c(t)$, can be calculated as [9]

$$\begin{aligned} u_c(t) =& \frac{1}{(2\pi\hbar)^{3NP} Z_P} \int\int \prod_{j=1}^{N} \prod_{k=1}^{P} dp_j^{(k)} dr_j^{(k)} \\ & e^{-\frac{\beta_T}{P} H_P(p_j^{(k)}, r_j^{(k)})} \frac{1}{Nm^2} \sum_{i=1}^{N} \bar{p}_i(0) \cdot \bar{p}_i(t), \end{aligned} \tag{3.23}$$

where $\bar{p}_i(t)$ is the momentum of the centroid of the ith polymer chain at time t, and β_T being the inverted temperature, $\beta_T = 1/(k_b T)$. The Hamiltonian, $H_n(p_j^k, r_j^k)$ is given by

$$\begin{aligned} H_P(p_j^k, r_j^k) =& \sum_{j=1}^{N} \sum_{k=1}^{P} \left(\frac{(p_j^{(k)})^2}{2m} + \frac{1}{2} m\omega_P^2 (r_j^{(k)} - r_j^{(k-1)})^2 \right) \\ & + \sum_{k=1}^{P} U(r_1^{(k)}, ...r_N^{(k)}). \end{aligned} \tag{3.24}$$

The canonical VACF is related to the normal VACF through a Kubo-transformation of its frequency distribution [8],

$$\rho(\omega) = \rho_c(\omega)\frac{\beta_T\hbar\omega}{1 - e^{-\beta_T\hbar\omega}}, \tag{3.25}$$

where $\rho(\omega)$ is the frequency distribution of the normal VACF, given by equation 3.7. $\rho_c(\omega)$ is the canonical frequency distribution, calculated in a similar way using the canonical VACF,

$$\rho_c(\omega) = \frac{1}{2\pi}\int_{-\infty}^{\infty} u_c(t)e^{-i\omega t}dt. \tag{3.26}$$

It is given by Guarini et al. [8] that for a quantum liquid like para-hydrogen, the canonical frequency distribution from equation 3.26 can be related to a frequency spectrum, $f(\omega)$, as

$$f(\omega) = \frac{2m\beta_T}{3}\rho_c(\omega) = \frac{m\beta_T}{3\pi}\int_{-\infty}^{\infty} u_c(t)e^{-i\omega t}dt. \tag{3.27}$$

This frequency spectrum can then be used in the Gaussian approximation in equation 2.22 to calculate the TSL.

In the present work, a molecular dynamics software called i-PI [27] is used to simulate a system of liquid hydrogen. An example module in the code exists that implements the RPMD method to calculate the canonical VACF. The code is further modified in this work to be able to apply it to a variety of systems.

3.7.3 The diffusion constant

The diffusion constant, D, in equation 2.27 can be determined by experiment. However it can also be calculated from the velocity auto-correlation function from an MD simulation. The exact quantum mechanical diffusion constant for liquid para-hydrogen is calculated from the canonical VACF [9] as

$$D = \frac{1}{3}\int_0^{\infty} u_c(t)dt. \tag{3.28}$$

It is noted by Miller and Manolopoulos [9], that the RPMD approximation of the diffusion constant becomes dependent on the dimensions of the system. This effect is not investigated in detail in the present work, but should be included in future development of the method.

Chapter 4

Results and discussion

For all the RPMD simulations, a cubic simulation box with periodic boundary conditions was used. The system was initiated in a cubic crystal structure and velocities sampled from a Boltzmann distribution. The system was equilibrated in an NVT ensemble for a number of time-steps until an equilibrium state was assured. The system was then put in an NVE ensemble and the trajectories were collected for a number of 1.5 ps simulations. The Kubo-transformed VACF was then calculated as the average over these trajectories. The static structure factor was calculated from trajectories from the equilibrium run, after equilibrium had set in. This was done to save time, as the big system size needed for a statistically reliable result meant long simulation times.

4.1 Static structure factor

To find the static structure factor, $S(Q)$, equation 3.3 was used, where the radial distribution function, $g(r)$, was calculated from the centroid trajectories output from the molecular dynamics simulation. In order to get higher statistical certainty of the results, a system of 8000 molecules was simulated at 17.1 K. The trotter number was taken as 16 to allow for a faster simulation time. Two smaller systems were investigated with 16 and 32 beads and no significant difference was seen in the radial distribution function. Hence 16 beads were deemed sufficient. At 15.7 K, a system of 4096 molecules was simulated. To improve the statistics, the systems were sampled a number of times during the equilibrium run and an average was taken for the radial distribution function over the number of sampled points. For 17.1 K this number of points was 50 and for 15.7 K, 117 points were used. The radial distribution function was calculated using the method described earlier and fitted to the function in equation 3.5. The radial distribution function at 17.1 K was fitted between approximately 6 and 13 ångström and at 15.7 K it was fitted between approximately 8 and 11

ångström. The radial distribution functions together with their fits are plotted in figures 4.1a and 4.2a. The data was replaced from the start of the fit by the fitted function, which was extended further in r. The extended pair distribution functions are shown in figures 4.1b and 4.2b. The static structure factor at 17.1 K is plotted in figure 4.3 and at 15.7 K in figure 4.4 together with experimental data points by Celli and Dawidowski, digitised from [23]. The low Q behaviour of the static structure factor was seen to be highly dependent on the fitting of the function in equation 3.5. To see what effect the fitting parameters would have, the total cross section was computed using a couple different fitting parameters for the static structure factor and only a minor effect was seen. Because the effect was deemed small, and there was no physical reasoning for one choice of fitting parameters over the other, the parameters were calibrated under two conditions: To resemble the experimental data digitised from [23] and that $(S(Q) - 1) > -1$.

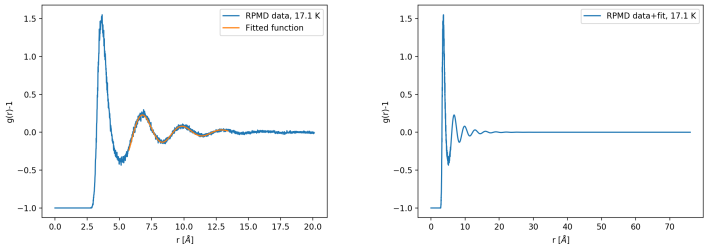

(a) 17.1 K (b) 17.1 K, extended

Figure 4.1: Radial distribution function at 17.1 K computed from RPMD, plotted together with fitted function from equation 3.5 (left) and extended onto a longer interval in r by the fitted function (right).

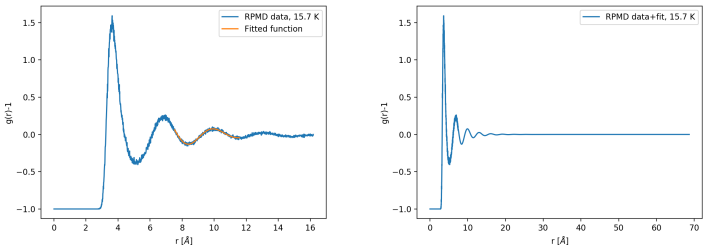

(a) 15.7 K (b) 15.7 K, extended

Figure 4.2: Radial distribution function at 15.7 K computed from RPMD, plotted together with fitted function from equation 3.5 (left) and extended onto a longer interval in r by the fitted function (right).

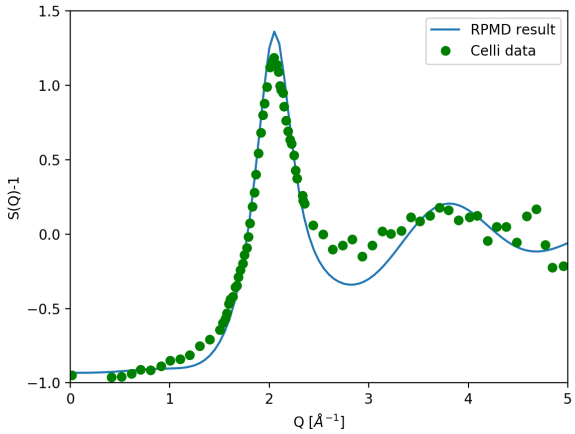

Figure 4.3: Static structure factor at $T = 17.1$ K, $n = 22.95$ nm^{-3} calculated from RPMD (line), compared to experimental data points digitised from [23], from the measurement by Celli et al. at $T = 17.1$ K, $n = 22.95$ nm^{-3} (green dots).

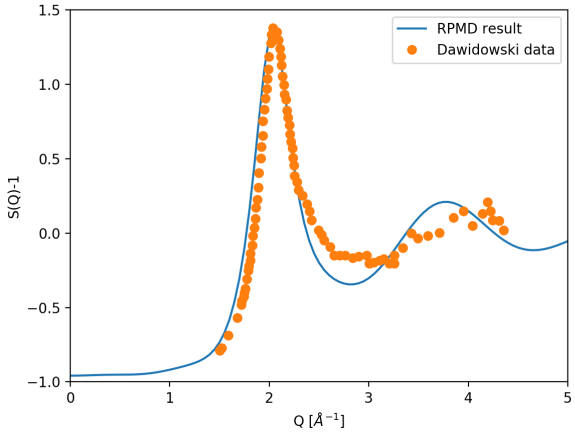

Figure 4.4: Static structure factor at $T = 15.7$ K, $n = 22.53$ nm^{-3} calculated from RPMD (line), compared to experimental data points digitised from [23], from the measurement by Dawidowski et al. at $T = 15.2$ K, $n = 22.71$ nm^{-3} (orange dots).

4.2 Velocity auto-correlation function

The Kubo-transformed, or canonical, VACF was computed for 61 trajectories of 15 ps and an average canonical VACF was taken. This was done for a system of 256 molecules with a Trotter number of 64. The canonical VACF can be seen in figure 4.5 compared to the canonical VACF computed by Guarini et al. using CMD [8]. There are some slight differences, which could because of differences between the RPMD and CMD methods. As Hone et al. discuss in [21], some small differences in the canonical VACF from RPMD and CMD are expected. However, it could also be related to the statistics used in computing the canonical VACF. Some variations in the computed canonical VACF were seen depending on the number of trajectories used to calculate the average canonical VACF. Test runs with a lower Trotter number were conducted with more trajectories in which there seemed to be a convergence after around 300 trajectories. The higher Trotter number used for 15.7 K means a higher computational load and only 61 trajectories could be used. In an ideal case, more trajectories would be computed and the overall results could be improved. However, for this project the agreement was considered to be reasonable and the statistics could be improved in the future if deemed necessary.

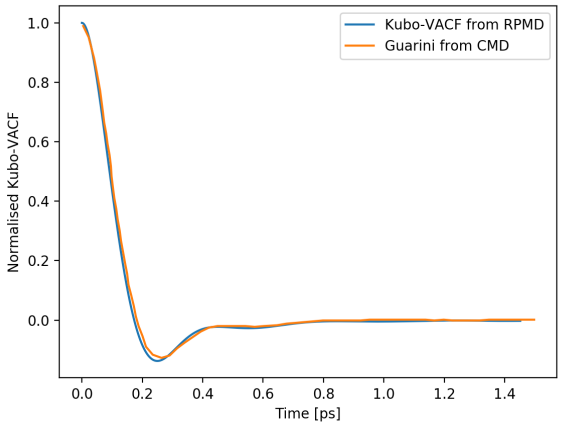

Figure 4.5: Kubo-transformed velocity auto-correlation function at $T = 15.7$ K, $n = 22.53$ nm^{-3} calculated from RPMD, compared to digitised results from Guarini et al. [8] using CMD for the same temperature and density.

To validate the method used to compute the canonical VACF using RPMD, bench-marking of the canonical VACF against other literature at other temperatures was also conducted. Miller and Manolopoulos [9] also used RPMD to compute the canonical VACF, and in figure 4.6 their result is digitised and plotted against the result of the present work at 14 K. The results from this project are seen to be comparable to their results. It is also noted that Miller and Manolopoulos [9] evaluated a system of 864 molecules while in the present work, a smaller system of 108 molecules were used at this temperature.

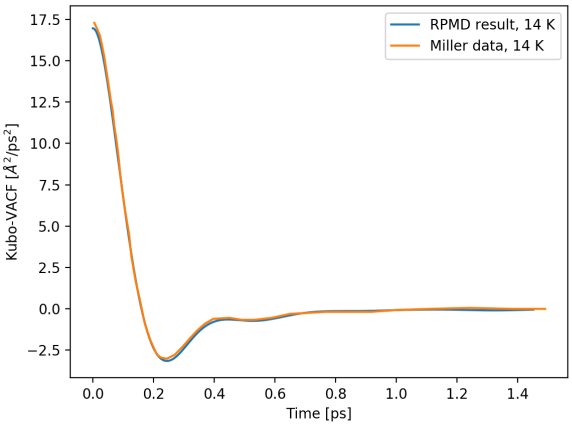

Figure 4.6: Kubo-transformed velocity auto-correlation function at $T = 14$ K, $n = 25.6$ nm^{-3} calculated from RPMD (blue line), compared to digitised results from Miller and Manolopoulos [9] using RPMD for the same temperature and density.

4.3 Frequency distribution

The canonical frequency distribution, $\rho_c(\omega)$, was calculated from the VACF using equation 3.26 and the frequency distribution, $\rho(\omega)$, was then calculated by equation 3.25. The frequency spectrum, $f(\omega)$ was calculated with equation 3.27. The method to calculate the frequency distribution was also bench-marked against the literature. In figures 4.7 and 4.8 $\rho(\omega)$ is compared to the results of a RPMD simulation conducted by Hone et al. [21] for $T = 14$ K and $T = 25$ K. The small deviations seen in our result compared to Hone could be an artefact of the lower statistics used for our data. Hone points out that in order to get a statistically significant result, 500 trajectories were sampled to calculate the average VACF. For the results presented here, only 80 trajectories were used at 14 K and 300 trajectories at 25 K, due to computational limitations. As a test, the frequency spectrum at 25 K was also computed using less trajectories and as expected, the deviations became more pronounced. In figure 4.9, the canonical frequency spectrum is plotted together with a diffusion component, calculated from equation 2.27. The diffusion component is subtracted from the frequency spectrum to get the 'solid-like' phonon distribution, $\rho_{solid}(\omega)$, that is used as an input to LEAPR. This phonon distribution is plotted in figure 4.10.

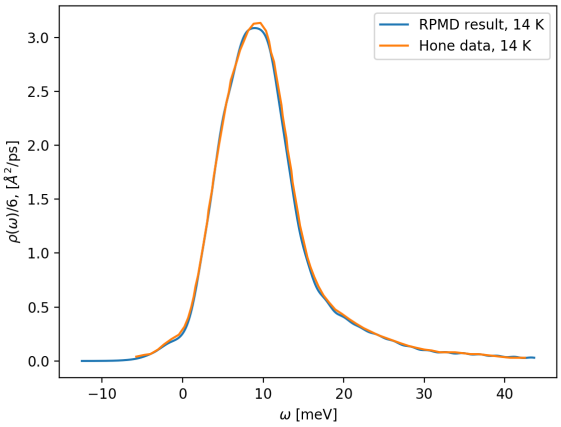

Figure 4.7: Frequency spectrum of the VACF computed from the canonical spectrum with equation 3.25 at $T =$ 14 K, compared to results from Hone et al. [21] at the same temperature.

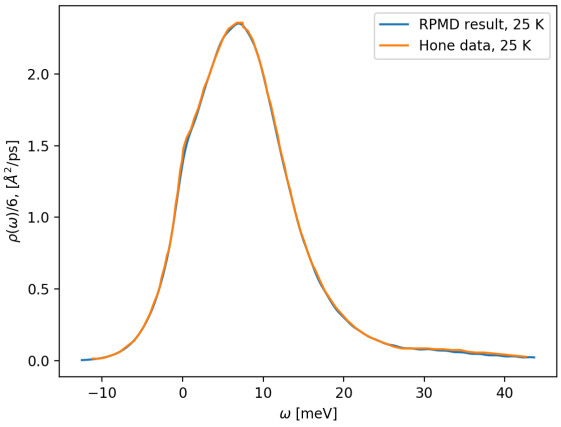

Figure 4.8: Frequency spectrum of the VACF computed from the canonical spectrum with equation 3.25 at $T =$ 25 K, compared to results from Hone et al. [21] at the same temperature.

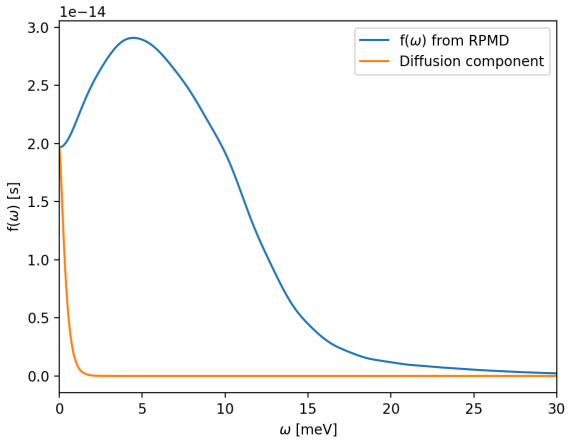

Figure 4.9: Frequency spectrum, f(ω), at $T = 15.7$ K. Computed from RPMD by equation 3.27. Also plotted is the diffusion component calculated from equation 2.27.

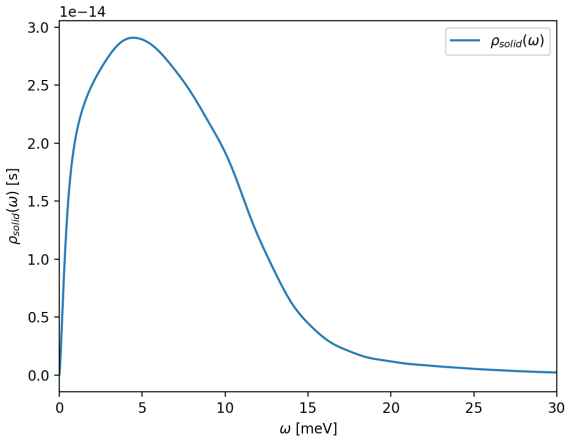

Figure 4.10: The solid-like phonon distribution, $\rho_{solid}(\omega)$, computed as the difference of the full frequency spectrum and the diffusion component from figure 4.9

Temperature	14 K	25 K
Present work, N=108	0.25 Å^2/ps	1.37 Å^2/ps
Miller, N=108	0.25 Å^2/ps	1.38 Å^2/ps

Table 4.1: Diffusion constants, D, calculated from RPMD in the present work, compared to Miller and Manolopoulos [9]. Calculated for a system of $N = 108$ molecules.

4.3.1 Diffusion component

The diffusion component is plotted in figure 4.9. To calculate the diffusion component, the dimensionless diffusion coefficient p was calculated from the diffusion constant, D, calculated from the canonical VACF using equation 3.28. The diffusion constant is compared to the diffusion constants calculated by Miller and Manolopoulos [9] in table 4.1. The results of the present work were shown to be comparable to [9] for a system of 108 molecules. However, it is noted by Miller and Manolopoulos [9], that there is a system size dependence of the diffusion constant computed from RPMD. The effect of this dependence on the total cross section was tested in the present work by scaling the diffusion constant and the frequency spectrum by a factor similar to [9], and no effect was seen. However, a future upgrade of the method could be to further investigate this dependence.

The dimensionless diffusion coefficient is given as an input variable in LEAPR. It is important in the present method that the coefficient is updated to be the same as the one used to calculate the diffusion component of equation 2.27 that is subtracted from the frequency spectrum. Note that in the NJOY manual [3] this variable is called c instead of p. For $T = 15.7$ K, the dimensionless diffusion coefficient is calculated as $p = 5.08$ and for $T = 20$ K, $p = 7.78$. These results are comparable to the value, $p = 6.3$, used by Granada and Gillete [6] in their evaluation of para-hydrogen at 15 K and 20 K.

The phonon expansion requires that the solid-like part of the phonon distribution behaves like ω^2 when $\omega \to 0$. However, after the subtraction of the diffusion component, a fitting of the first five points in the frequency spectrum to an ω^2-like function showed no notable difference in the final calculated cross section. Therefore it is assumed that the frequency spectrum, after subtracting the diffusion component, already exhibits an ω^2-like behaviour as $\omega \to 0$ that is good enough for the phonon expansion in LEAPR. Further investigation of this ω^2-like condition could be of interest in the future, to test it's limits and the effect on the total cross section.

4.4 Total inelastic cross section

The total inelastic cross section is calculated in NJOY with the input frequency distribution and static structure factor from the molecular dynamics simulations. The cross section is calculated in the H2D2-model with the Sköld approximation.

The free atom scattering cross section, σ_f, contained in the input variable *spr* is given by equation 2.12. With $\sigma_b = 82.03$ for hydrogen, taken from NIST [12], the input parameter is given by $spr = 20.505$. The coherent fraction, given in the variable $cfrac$ is calculated taking $\sigma_b = 82.03$ and $\sigma_{coh} = 1.7583$ from NIST, as $cfrac = 0.021$. The parameter twt, containing the weight factor for the diffusion part (also mentioned as w_t in the present report) is taken as $twt = 0.0125$ according to [6], leaving the weight for the solid-like part, $tbeta = 0.4875$.

Using these input parameters, the total inelastic cross section for three energy ranges is plotted in figures 4.11, 4.12 and 4.13 compared to the simulation results from Guarini et al. [8] and experimental data by Celli et al. [29], Grammer et al. [30] and Seiffert [31], digitised from [8]. With these results, it is shown that the method can be used to produce a total cross section from quantum molecular dynamics with similar results to available experimental data. Some differences are seen between the results from this thesis and the results of the simulations by Guarini et al. [8]. These observed differences may be related to the implementation of the Egelstaff-Schofield diffusion component in LEAPR. This could be explored further by, for instance, adjusting the diffusion weight in equation 2.27, as this parameter was seen to have an effect on the total cross section. It would also be interesting to see in the future if the LEAPR code could be updated to give an option to skip the Egelstaff-Schofield diffusion component. Then the full frequency distribution given by MD simulations could be used as an input and perhaps the cross section compares better to the experimental data.

In the high energy range in figure 4.13, some differences are seen between the present results and the Guarini et al. [8] CMD+GA model. However, these differences were not investigated in detail in the present work.

In the low energy range in figure 4.11, a difference is also seen between our result and the Guarini CMD+GA model [8]. Since this is the energy range in which the Sköld approximation is used to account for the coherent scattering, a possible reason could be related to the use of the RPMD calculated static structure factor, $S(Q)$, instead of one based on experimental data, as used in Guarini et al. [8]. A suggestion for future development of the method is to further investigate the use of experimental data for $S(Q)$ to see if the agreement to Guarini et al. [8] improves.

Guarini et al. [8] calculates the cross section directly from the molecular dynamics results, without the use of the NJOY code. An effort to follow the same calculations was made during this project. However, the integration in the Gaussian approximation was too numerically heavy for the scope of this project. With a better understanding of numerical integration, a further study could be to calculate the cross section directly from the molecular dynamics results to find out if the differences in the cross section comes from the molecular dynamics or from the implementations in NJOY.

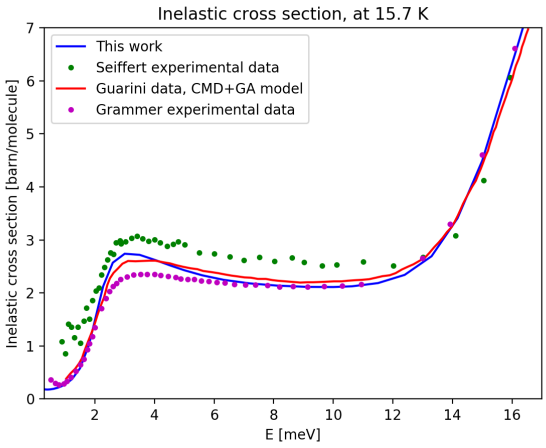

Figure 4.11: The total inelastic cross section at $T = 15.7$ K in the low energy range between 0-16 meV. Results from NJOY using the inputs from RPMD compared to experimental data and simulation results digitised from Guarini et al. [8].

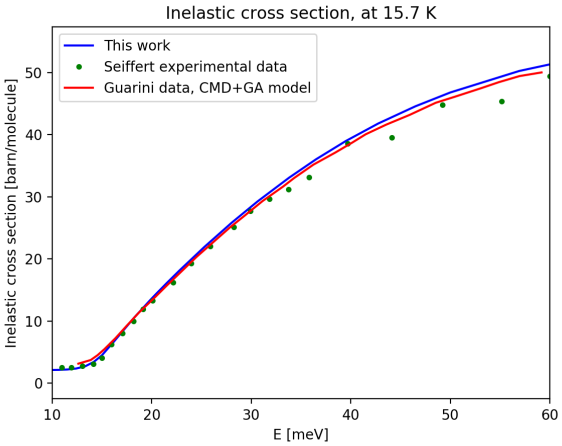

Figure 4.12: The total inelastic cross section at $T = 15.7$ K in the medium energy range between 10-60 meV. Results from NJOY using the inputs from RPMD compared to experimental data and simulation results digitised from Guarini et al. [8].

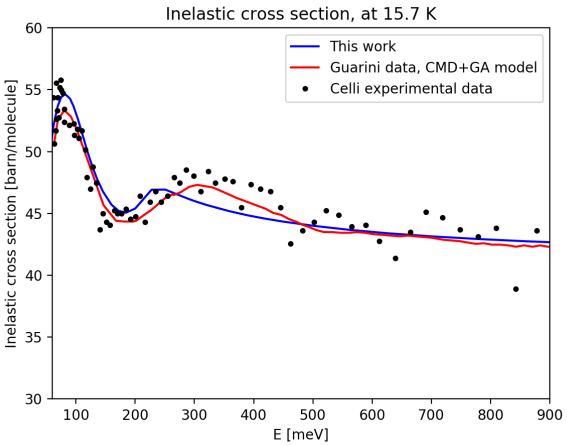

Figure 4.13: The total inelastic cross section at $T = 15.7$ K in the high energy range between 60-900 meV. Results from NJOY using the inputs from RPMD compared to experimental data and simulation results digitised from Guarini et al. [8].

Chapter 5

Conclusions

In the present report, it has been shown that the new method of calculating the scattering kernels using inputs from QMD can be implemented and give results comparable to existing literature. It is noted that the differences from this method compared to previous work based solely on QMD, could be related to a number of different sources. These include for example, the usage of the QMD calculated static structure factor as opposed to one based on measured data, the statistics of the simulation results, and effects related to the diffusion model used in NJOY. For future upgrades of the method, it would be of interest to take further advantage of modern parallel programming techniques, to not only increase statistics, but to also possibly update NJOY to avoid the usage of the phonon expansion, thereby using directly results from molecular dynamics simulations. Overall the method worked as intended and could be used in future scattering kernel calculations at the ESS.

Bibliography

[1] European Spallation Source, "Home page," European Spallation Source. [Website] Available: https://europeanspallationsource.se/, Accessed on: March 20, 2020

[2] L. Zanini et al., "Design of the cold and thermal neutron moderators for the European Spallation Source," Nuclear Inst. and Methods in Physics Research, vol. A 925, pp. 33–52 2019. Accessed on: March, 29, 2020. doi: https://doi.org/10.1016/j.nima.2019.01.003, [Online].

[3] R. E. MacFarlane, et al. The NJOY Nuclear Data Processing System, Version 2016. (2016) [Online]. Place: Los Alamos National Laboratory. Available: https://www.njoy21.io/NJOY2016/, Accessed on: March, 29, 2020.

[4] Nuclear Energy Agency, "Thermal Scattering Law S(α,β): Measurement, Evaluation and Application," International Evaluation Co-operation, Volume 42, 2020. Available: https://www.oecd-nea.org/science/wpec/documents/volume42.pdf, Accessed on: March, 29, 2020.

[5] J. I. Márquez Damián, "NJOY H2D2, Git page." GitHub. Available: https://github.com/marquezj/NJOY2016/tree/H2D2, Accessed on: March. 29, 2020.

[6] J. R. Granada, V. H. Gillete, "A New Thermal Neutron Scattering Kernel for Liquid Hydrogen," Physica vol. B 348 pp. 6-14, 2004. Accessed on: March, 29, 2020. doi: https://doi.org/10.1016/j.physb.2003.07.008, [Online].

[7] J. I. Márquez Damián, et al., "Generation of thermal scattering libraries for liquids beyond the Gaussian approximation using molecular dynamics and NJOY/LEAPR," Ann. Nucl. En. vol. 92, pp. 107-112, 2016. Accessed on: March, 29, 2020. doi: https://doi.org/10.1016/j.anucene.2016.01.036, [Online].

[8] E. Guarini, et al., "Velocity Autocorrelation in liquid parahydrogen by quantum simulations for direct parameter-free computations of neutron cross

sections," Physical review vol. B 92, no. 104303, 2015. Accessed on: March, 29, 2020. doi: https://doi.org/10.1103/PhysRevB.92.104303, [Online].

[9] T. F. Miller and D.E Manolopoulos, "Quantum diffusion in liquid para-hydrogen from ring-polymer molecular dynamics," J. Chem. Phys. vol. 122, no. 184503, 2005. Accessed on: March, 29, 2020. doi: https://doi.org/10.1063/1.1893956, [Online].

[10] G. I. Bell, S. Glasstone, Nuclear Reactor Theory. Washington DC, US. US Atomic Energy Commission, 1970.

[11] G. L. Squires, Introduction to the Theory of Thermal Neutron Scattering. Cambridge, UK. Cambridge University Press, 1996.

[12] National Institute of Standard and Technology, "Home page", National Institute of Standard and Technology. [Website] Available: https://www.nist.gov/. Accessed on: March 20, 2020.

[13] B. T. M. Willis, C. J. Carlile, Experimental Neutron Scattering. New York, US. Oxford University Press, 2009.

[14] G. H. Vineyard, "Scattering of Slow Neutrons by a Liquid," Phys. Rev. vol. 110, no. 999, 1958. Accessed on: April, 7, 2020. doi: https://doi.org/10.1103/PhysRev.110.999, [Online]

[15] K. Skold, "Small Energy Transfer Scattering of Cold Neutrons from Liquid Argon," Phys. Rev. Let. vol. 19, no. 18, 1967. Accessed on: March, 29, 2020. doi: https://doi.org/10.1103/PhysRevLett.19.1023, [Online]

[16] J. A. Young and J. U. Koppel, "Slow Neutron Scattering by Molecular Hydrogen and Deuterium," Phys. Rev. vol. 135, no. A603, 1964. Accessed on: March, 29, 2020. doi: https://doi.org/10.1103/PhysRev.135.A603, [Online].

[17] E. Guarini, "The Neutron Double Differential Cross-Section of Simple Molecular Fluids: Refined Computing Models and Nowadays Applications," J. Phys.: Condens. Matter vol. 15 pp. R775-R812, 2003. Accessed on: March, 29, 2020. doi: https://doi.org/10.1088/0953-8984/15/19/204, [Online].

[18] J. Keinert and J. Sax, "Investigation of Neutron Scattering Dynamics in Liquid Hydrogen and Deuterium for Cold Neutron Sources," Kerntechnik vol. 51, no. 19, 1987.

[19] P. A. Egelstaff and P. Schofield, "On the Evaluation of the Thermal Neutron Scattering Law," Nuclear Science and Engineering, vol. 12:2, pp. 260-270 1962. Accessed on: March, 29, 2020. doi: https://doi.org/10.13182/NSE62-A26066, [Online].

[20] J. I. Márquez Damián, et al., "An Evaluation of the Scattering Law for Light and Heavy Water in ENDF-6 Format, Based on Experimental Data and Molecular Dynamics," Nuclear Data Sheets vol. 118 pp. 169–171, 2014. Accessed on: March, 29, 2020. doi: https://doi.org/10.1016/j.phpro.2014.11.040, [Online].

[21] T. D. Hone, et al., "A comparative study of imaginary time path integral based methods for quantum dynamics," J. Chem. Phys. vol. 124, no. 154103, 2006. Accessed on: March, 29, 2020. doi: https://doi.org/10.1063/1.2186636, [Online].

[22] R. Lesar. Introduction to Computational Materials Science, Fundamentals to Applications, Cambridge, UK. Cambridge University Press, 2013.

[23] M. Celli, et al., "Microscopic structure factor of liquid hydrogen by neutron-diffraction measurements," Physical Review vol. B 71, no. 014205, 2005. Accessed on: March, 29, 2020. doi: https://doi.org/10.1103/PhysRevB.71.014205, [Online].

[24] J. Dawidowski, et al., "Static structure factor of liquid parahydrogen," Physical Review vol. B69, no. 014207, 2004. Accessed on: March, 29, 2020. doi: https://doi.org/10.1103/PhysRevB.69.014207, [Online].

[25] M. E. Tuckerman, Stat. Mech.: Theory and Molecular Simulation. New York, US. Oxford University Press, 2010.

[26] N. D. Kondratyuk, et al., "Quantum nuclear effects in water using centriod molecular dynamics," Journal of Physics: Conference Series vol. 946, no. 012109, 2018. Accessed on: March, 29, 2020. doi: 10.1088/1742-6596/946/1/012109, [Online].

[27] Kapil et al., "i-PI 2.0: A universal force engine for advanced molecular simulations," Comp. Phys. Comm. vol. 236, pp. 214–223, 2018. Accessed on: March, 29, 2020. doi: https://doi.org/10.1016/j.cpc.2018.09.020, [Online].

[28] NNDC, Brookhaven National Laboratory. ENDF/B-VIII.0 Evaluated Nuclear Data Library. (2020) [Online]. Brookhaven National Laboratory. Available: https://www.nndc.bnl.gov/endf/b8.0/. Accessed on: March, 29, 2020.

[29] M. Celli, et al., "The total neutron cross section of liquid para-hydrogen," Journal of Physics: Cond. Matter, vol. 11, no. 50, 1999. Accessed on: April, 22, 2020. doi: http://dx.doi.org/10.1088/0953-8984/11/50/315 [Online].

[30] K. B. Grammer, et al., "Measurement of the scattering cross section of slow neutrons on liquid parahydrogen from neutron transmission," Physical review vol. B 91, no. 180301(R), 2015. Accessed on: April, 22, 2020. doi: https://doi.org/10.1103/PhysRevB.91.180301 [Online].

[31] W. D. Seiffert, Euroatom Report No. EUR 4455d, 1970 (unpublished).